

Article

Land Subsidence Evolution and Simulation in the Western Coastal Area of Bohai Bay, China

Can Lu ^{1,2} , Lin Zhu ^{1,2,*}, Xiaojuan Li ^{1,2}, Huili Gong ^{1,2}, Dong Du ³, Haigang Wang ^{4,5} and Pietro Teatini ⁶

- ¹ College of Resource Environment and Tourism, Beijing Laboratory of Water Resources Security, Laboratory Cultivation Base of Environment Process and Digital Simulation, Capital Normal University, Beijing 100048, China
 - ² Key Laboratory of Mechanism, Prevention and Mitigation of Land Subsidence, MOE, Capital Normal University, Beijing 100048, China
 - ³ China Geological Survey, North China Center for Geoscience Innovation Precambrian Research Center, Tianjin 300170, China
 - ⁴ China Institute of Geo-Environment Monitoring, Beijing 100081, China
 - ⁵ Hebei Cangzhou Groundwater and Land Subsidence National Observation and Research Station, Cangzhou 061000, China
 - ⁶ Department of Civil, Environmental and Architectural Engineering, University of Padova, 35121 Padova, Italy
- * Correspondence: lin.zhu@cnu.edu.cn

Abstract: Groundwater overexploitation and loading of buildings have been the main factors triggering land subsidence along the west coast of Bohai Bay, China, since the 2000s. Uneven subsidence has been causing damage to buildings and civil facilities, loss of elevation, increasing the risk of flood and seawater intrusion, and threatening the safety of people's lives and property. This paper analyzed the spatial and temporal features of land subsidence along the coastal area from 2003 to 2010 and from 2015 to 2020, respectively. The relations between the initiating factors and land subsidence were explored. Then, the simulation model of land subsidence was constructed through a deep learning method. During the process, multiple data were collected, including land satellite (Landsat), environmental satellite advanced synthetic aperture radar (ENVISAT ASAR) and Sentinel-1 images, leveling data, lithological data, and groundwater level data. The area occupied by buildings and vertical displacement were extracted by using supervised classification, small baseline subset (SBAS), and persistent scatterer interferometry (PSI) technologies. The gated recurrent unit (GRU) neural network was adopted to simulate the evolution of land subsidence. Results showed that the maximum annual vertical displacement rate decreased from -94 mm/yr during 2003–2010 to -87 mm/yr during 2015–2020. The correlation efficiency between the groundwater level of the third confined aquifer group and land subsidence was larger than the area occupied by buildings and the compressible layer thickness with subsidence. The constructed GRU neural network model can simulate subsidence from September 2019 to December 2019, with the overall RMSE and MAE being 3.16 mm and 2.19 mm, respectively. This work can facilitate an understanding of the evolution and prevention of land subsidence along the west coast of Bohai Bay, which will provide information for policy decisions and flood-fighting plans of the worldwide coastal cities.

Keywords: land subsidence; urbanization; groundwater overexploitation; GRU; InSAR



Citation: Lu, C.; Zhu, L.; Li, X.; Gong, H.; Du, D.; Wang, H.; Teatini, P. Land Subsidence Evolution and Simulation in the Western Coastal Area of Bohai Bay, China. *J. Mar. Sci. Eng.* **2022**, *10*, 1549. <https://doi.org/10.3390/jmse10101549>

Academic Editor: Tom Spencer

Received: 17 September 2022

Accepted: 16 October 2022

Published: 20 October 2022

Publisher's Note: MDPI stays neutral with regard to jurisdictional claims in published maps and institutional affiliations.



Copyright: © 2022 by the authors. Licensee MDPI, Basel, Switzerland. This article is an open access article distributed under the terms and conditions of the Creative Commons Attribution (CC BY) license (<https://creativecommons.org/licenses/by/4.0/>).

1. Introduction

More than 200 land subsidence areas have been reported caused by excessive exploitation of groundwater, most of which belong to alluvial basins or coastal plains [1]. In coastal areas, land subsidence makes them more vulnerable to floods and sea level rise, which may cause the inundation of deltas, enhancing coastal erosion and seawater intrusion [2–4]. Spatially dense and continuous observation of land subsidence improved understanding of the driving mechanisms, and reliable predictions of future subsidence are needed for policy decisions and flood-resilience plans for coastal megacities around the world.

Monitoring land subsidence is the base for studying land subsidence. Compared with conventional technologies, including leveling, GNSS, and extensometer, Interferometric Synthetic Aperture Radar (InSAR) technology can be used to obtain large-scale land subsidence with a relatively high spatial resolution with millimetric accuracy. The InSAR technique uses microwave radar signals to illuminate the ground surface and then records the amplitude and phase of the signals backscattered from the surface. Comparing the change in the phase enables the displacement of the ground surface toward or away from the sensor to be determined. The precision of the phase observations is often expressed in terms of the coherence between the two SAR images, with values close to one indicating high-quality measurements. The radar wavelength of the SAR instrument, atmospheric conditions during each image acquisition, and land cover can affect the interferometric coherence. Loss of coherence can limit the coastal areas for which conventional InSAR can provide useful data. Multitemporal InSAR approaches have been developed to overcome the limitations of loss of coherence. The commonly used InSAR time series techniques include persistent scatterer interferometry (PSI) and the small baseline subset (SBAS) method, which can minimize traditional InSAR limitations, including spatial and temporal decorrelation and atmospheric effect [5,6]. Interferometric Point Target Analysis (IPTA) was carried out on 59 ERS SAR data from 1992 to 2000 to investigate the displacement in Venice coastland with accuracy on the order of 1–2 mm/yr [7]. The PSI method was used to monitor the land subsidence in Jakarta, Indonesia, with ALOS PALSAR images from 2007 to 2010. The two subsidence bowls in Jakarta had subsided up to 865 mm. The standard deviation between the derived subsidence rate and the GPS-measured value was 9 mm/yr [8]. PSI technology was adopted for dealing with the Sentinel-1 images to get land subsidence in Tianjin from 2015 to 2018. More than 95% of the persistent scatterer showed the absolute difference between the derived displacement and the leveling data within 5 mm [9]. SBAS technology was applied to dealing with 25 Sentinel-1 images from 2015 to 2016 to investigate subsidence in the Binhai New Area, Tianjing. The vertical displacement rate ranged from –70 to 10 mm/yr [10]. However, considering coastal land subsidence is a complex long-term developing process, it is difficult to find the evolution mechanism on the basis of short-term monitoring.

Land subsidence is complex in coastal areas due to the sediment's natural consolidation, groundwater pumping, and build-up areas' load. A striking linear relationship between compaction rate and peat thickness on the basis of ~250 boreholes found in Mississippi Delta [11]. It was found that subsidence is mainly caused by the primary compaction of the Holocene strata in Po Delta [12]. Land subsidence was concentric around locations of intense groundwater withdrawal in Houston–Galveston, Gulf Coast region of the United States [13]. Subsidence with a value up to 140 mm/yr due to peat compaction and oxidation was quantified in built-up areas in the Rhine–Meuse delta in the Netherlands on the basis of borehole data and dry bulk density, organic matter, and CO₂ respiration [14]. Previous studies showed that the main causes of land subsidence in the Binhai New Area are intensive groundwater extraction, the natural consolidation of cohesive soil, and building load [15]. The research found that the land subsidence rate of Tianjin coastal towns varied with the type of land use, and the subsidence of industrial areas was more serious due to the overexploitation of groundwater [16]. The in situ test indicated that with the same groundwater exploitation, the land subsidence was more serious where the clay thickness was thicker [17]. The extensometer data from 2011 to 2014 was used and found that land subsidence at 33 m depth accounted for ~70% of total land subsidence, which indicated that urban development played the important contributor to land subsidence in Tianjin's coastal region [18].

Modeling land subsidence is essential for geo-disaster prevention, generally, including physics-based models and data-based models. Physics-based model is based on the physical process of land subsidence, which requires many input data such as hydrogeological and geotechnical parameters, initial conditions, and boundary conditions. Physics-based subsidence model generally is fit for small-scale areas. The data-based model includes an

autoregressive model (AR), gray model (GM), artificial neural network model, and deep learning model. AR model and GM model are based on historical subsidence data, which makes the prediction accuracy not high and easily overfitting. Artificial neural network models such as the backpropagation (BP) model, coupled genetic algorithm (GA) and BP model, and eXtreme gradient boosting (XGBoost) model consider the influencing factors of land subsidence, but the convergence speed is slow [19,20]. Long short-term memory (LSTM) and gated recurrent unit (GRU) belong to a recurrent neural network, which can learn the characteristics of time series data, share parameters during the time domain using a cyclic structure (memory unit), record the context of the sequence and process long-term data with nonlinear characteristics [21,22]. A geographically weighted LSTM (GW-LSTM) model was proposed for effectively simulating the subsidence in the Chaobai River alluvial fan in the northeast Beijing Plain area, China [23]. The GRU model uses an update gate to replace the input gate and output gate used in the LSTM model, which can improve the network training efficiency, require fewer parameters, and low requirement for computing resources. GRU models have been widely used in behavior prediction, machine translation, and text classification [24]. In the field of land subsidence, the GRU model was used to predict the deformation induced by shield tunneling [25]. The result is better than the outputs from the BP model. However, few studies have applied the GRU model to the subsidence caused by groundwater exploitation.

The Binhai New Area in Tianjin Municipality is located on the west bank of Bohai Bay, which has been one of the most rapidly developing areas in China since 2006, with the issued development and opening-up policy. Since the 1950s, groundwater has been intensively exploited to meet the demands of rapid economic development and population growth, which produce severe subsidence problems in the Binhai New Area [26]. Over the past decades, many scholars have studied the evolution, factors of land subsidence, and land subsidence modeling. The existing studies aimed at a single factor affecting land subsidence in coastal areas, and the constructed data-based models do not consider the comprehensive interaction of multiple variables.

The objectives of this paper are to explore the evolution characteristics of land subsidence from 2003 to 2020 and to provide an effective method to simulate land subsidence in the Binhai New Area on the west coast of Bohai Bay, China. The relations between land subsidence and three main factors, including groundwater level changes in the aquifer system, building load, and geological features, were analyzed. Then, the GRU model was constructed to simulate land subsidence with the three factors as input data. The results can supply scientific support for decision-makers to establish hazard mitigation measures and groundwater resource management in the Binhai New Area and supply technologies for other coastal cities that are currently experiencing land subsidence problems.

2. Study Area

The study area is the Binhai New Area, one of the important harbors for northern China, located on the west coast of Bohai Bay, Tianjin municipality. It consists of Hangu District, Tanggu District, and Dagang District. The total area is 2270 km², and the length of the western coastline is about 150 km (Figure 1). This region belongs to a warm temperate monsoon continental climate with an annual average temperature of 13 °C and precipitation of 566 mm from 1956 to 2020. The terrain is generally flat, with an elevation of 2.6–4.5 m. Rivers, canals, and lakes are widely distributed. The Hai River, Jiyun Canal, Chaobai River, and Duliujian River merge into the sea in this area.

The Quaternary sediments, with a thickness ranging from 280 to 450 m, are composed of four main aquifer units (Figure 2). From west to east, the sediments become finer, and permeability gradually decreases. The thickness of low permeability layers increases, and groundwater quality gradually becomes saline. Groundwater in the first aquifer group is mainly unexploited saltwater. The underlying aquifer groups (from the second to the fourth) are deep confined groundwater systems and are composed of freshwater. The most exploited groundwater is from the third confined aquifer group [27,28].

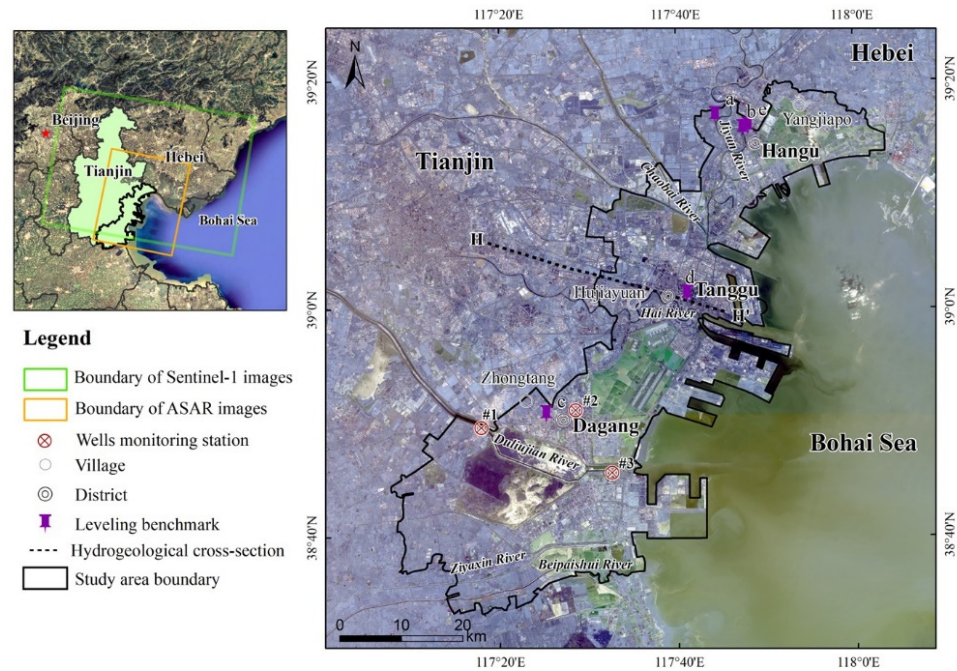


Figure 1. Distribution of the study area. The yellow box indicates the boundary of the ENVISAT ASAR images (track 175, frame 2817), and the green box indicates the boundary of the Sentinel-1 images (path 149, frame 463) used to map land subsidence. The positions of the leveling benchmarks and wells monitoring station are provided. The black dashed line shows the hydrogeological cross-section. The background is a Sentinel-2 image acquired on 16 September 2020.

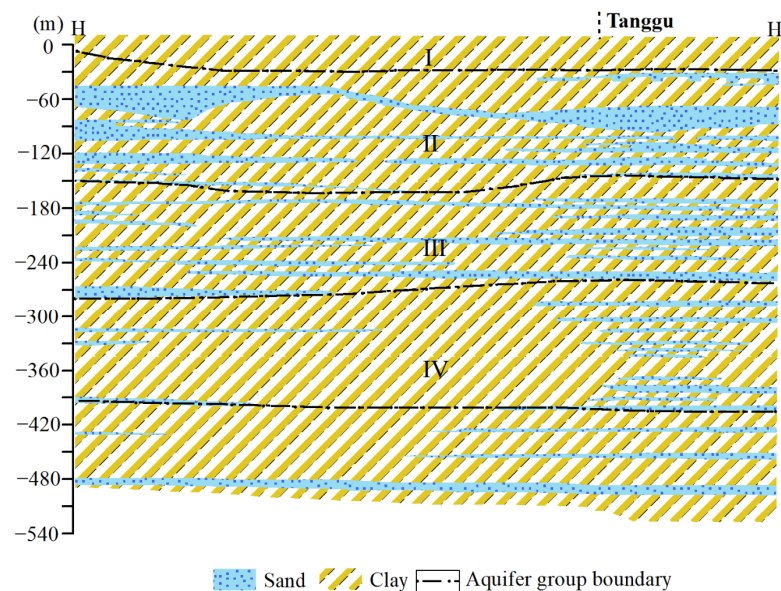


Figure 2. Hydrogeological cross-section in the study area. The black dashed line represents the aquifer group boundary (modified from [29]).

Water consumption increased with urbanization. Groundwater has been pumped since the beginning of the previous century. In the 1980s, the annual pumping volume was $1.4 \times 10^8 \text{ m}^3$. After the operation of the water diversion project from Luan River to Tianjin in 1983, the pressure from industrial and residential water demands was partially alleviated. The annual pumping of groundwater decreased to $0.6 \times 10^8 \text{ m}^3$ in the early 2000s. In 2002, the groundwater pumping volume of the second, third, and fourth confined aquifer

groups in the Binhai New Area was $2.1 \times 10^7 \text{ m}^3/\text{a}$, $3.5 \times 10^7 \text{ m}^3/\text{a}$, and $1.7 \times 10^7 \text{ m}^3/\text{a}$, respectively, the pumping volume of the third confined aquifer group was more.

Land subsidence has been observed in Tanggu District in the center part of the study area since 1952 [27]. Due to the increase in groundwater exploitation, the displacement rate obtained by leveling reached $-30 \sim -50 \text{ mm/yr}$ from 1960 to 1966. From 1967 to 1985, the displacement rate in Tanggu District increased largely, with a range of -80 to -150 mm/yr . After 1986, Tianjin municipality carried out land subsidence controlling implements, which diverted Luanhe River water to reduce groundwater exploitation. The groundwater level in the second confined aquifer group had recovered $\sim 24 \text{ m}$ from 1986 to 1996, with the land subsidence rate correspondingly decreased [30,31]. From 2005 to 2013, the displacement rate in Tanggu District ranged from -19 to -35 mm/yr , among which the land subsidence at the urban construction area and sea reclamation area was large. From 2015 to 2016, the land subsidence due to urban construction was small, and there was almost no subsidence in Tanggu District [10].

The maximum subsidence in Hangu District from 1957 to 2006 was 3.11 m, and the average subsidence in 2006 was 27 mm. From 2015 to 2016, the displacement rate in Hangu District reached -70 mm/yr , and the subsidence bowl was located in Yang jiapo town. The maximum subsidence in Dagang District from 1959 to 2006 was 1.45 m, and the average subsidence in 2006 was 33 mm. Zhongtang town had a large subsidence, with a maximum subsidence of 66 mm [32].

3. Materials and Methods

3.1. Materials

In order to explore the evolution characteristics of land subsidence, find out the relations between land subsidence and three main factors, to provide an effective method to simulate land subsidence, the data used in this article mainly include remote sensing data and thematic data. Among them, remote sensing data includes radar data and optical remote sensing data. The thematic data mainly includes leveling data, the contour lines of groundwater level depth, the third confined groundwater level at three long-term observation wells, and the schematic description of two observation wells lithologies. The flowchart of the processing is shown in Figure 3.

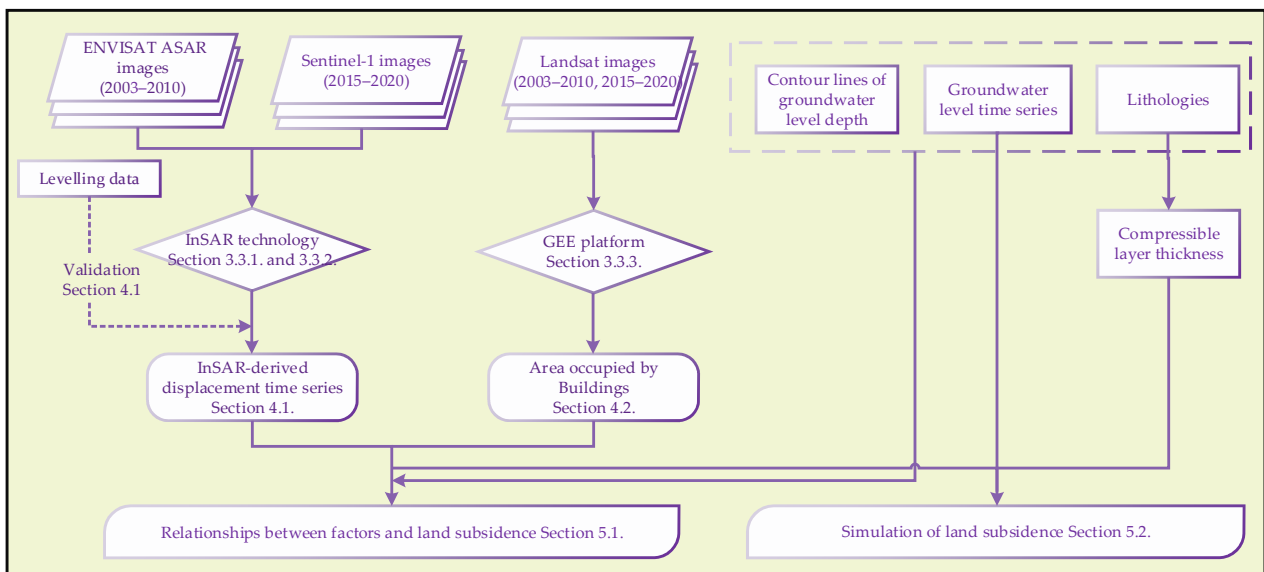


Figure 3. The flowchart of the processing.

3.2. Dataset

3.2.1. Remote Sensing Data

There were 27 Stripmap-mode descending ENVISAT ASAR images with a revisit time of 35 days from 2003 to 2010 and 66 descending TOPS-mode Sentinel-1 images with a revisit time of 12 days from 2015 to 2020 that were collected. The two types of SAR images were obtained with C-band sensors. These images were processed to obtain the distribution of land subsidence by using InSAR technology.

Optical images, including Landsat 5 and Landsat 8 images, were used to extract the area occupied by buildings on the basis of the Google Earth Engine (GEE). The study area was covered by two Landsat scenes. A total of 452 images from 2003 to 2010 and 2015 to 2020 were selected.

3.2.2. Thematic Data

Five leveling benchmarks provided by authorities were obtained from precision geometric leveling to validate the accuracy of the InSAR-based land subsidence. The distribution is given in Figure 1. There were two leveling benchmarks from 2003 to 2005 and three benchmarks from 2017 to 2019.

The groundwater level depth recorded the distance from groundwater to the surface. The contour lines of groundwater level depth below the land surface of the second and third confined aquifer groups in 2013, 2016, and 2019 were collected to understand the relationship between land subsidence and groundwater level. The monthly groundwater level of the third confined aquifer group was collected at three groundwater monitoring wells from January 2018 to December 2019, which were used for simulating the subsidence.

Schematic descriptions of two groundwater monitoring wells lithologies were collected to analyze the relationship between the compressible layers thickness and land subsidence.

3.3. Methodology

3.3.1. Land Subsidence from 2003 to 2010 with SBAS Technology

Considering that the ASAR images number from 2003 to 2010 were limited, the time interval of images was long, which may cause spatiotemporal incoherence. SBAS technology was used to deal with the ASAR images. SBAS methodology was proposed by Berardino et al. [6], which can guarantee high land subsidence monitoring accuracy with limited images. This method can support multitemporal images and utilize interferometric pairs with small spatial and temporal baselines. The main processing steps were described as follows.

First, interferograms were generated from single-look complex images. Among all the possible interferograms formed by pairs of images, 60 interferograms from SAR images were selected for further processing by setting thresholds for spatial and temporal baselines with values of 400 m and 400 days, respectively. The external Shuttle Radar Topography Mission digital elevation model with 30 m resolution was used to remove the topographic component of the interferometric phase and geocode the interferograms.

Second, after eliminating the noise phase using an adaptive filter, the minimum cost flow method was used for phase unwrapping, with a coherence threshold of 0.4. The reason for setting the coherence threshold to 0.4 is that the time interval of Envisat ASAR images is too long. After many experiments, the results obtained by setting the coherence threshold to 0.4 have been verified to be good. The next step was estimating the land subsidence rate by stacking multiple unwrapped differential interferograms.

Third, high-coherence candidate points were generated from all high-coherence pixels, and atmospheric effects were removed with a spatiotemporal filtering method. After removing the elevation, atmospheric, and noise errors from the interference phase, the deformation phase results in the line of sight direction were obtained.

3.3.2. Land Subsidence from 2015 to 2020 with PSI Technology

Considering PSI technology can overcome the problems of traditional InSAR systems related to temporal and geometrical decorrelation and minimize atmospheric and noise phases, PSI technology was used to process 66 Sentinel-1 images from 2015 to 2020 [33,34].

First, the single master image (acquired on 2 March 2017) was chosen from SAR images based on the short spatial baseline, temporal baseline, and Doppler centroid frequency difference. Then, a series of interferograms was constructed, and persistent scatterers (PSs) with temporal coherence and phase stability were obtained by using the model coherence and amplitude standard deviation threshold.

The differential interferometric phase of each PS in the interferogram is the accumulation of five components, including the deformation phase along the line of sight, the topographic phase, the phase component due to atmospheric delay, the orbital error phase, and the phase noise. The orbital error phase was mitigated by refining the satellite baselines with the least-squares approach based on unwrapped phases. The terrain heights were extracted using Shuttle Radar Topography Mission digital elevation model with 30 m resolution. The phase component associated with atmospheric delays and the phase noise were removed based on temporal frequency characteristics [7,35]. Finally, the line-of-sight deformation phase was obtained.

3.3.3. Building Information Using the GEE

Building load can affect land subsidence to some extent in the alluvial plain [19], which effect may be obvious in the coastal area. The GEE is a cloud-based computing platform on which users can deal with available remotely sensed images using a web-based Integrated Development Environment code editor without downloading these data to the local machines [36]. A total of 452 images were selected for extracting building information. Notably, if users do not specifically select the path and row numbers of a scene, all the images that intersect with the boundary of the study area will be automatically selected on the GEE platform.

The top-of-atmosphere (TOA) reflectance data of Landsat 5 and Landsat 8 images in the study area were chosen by setting the boundary. Then, the quality assurance (QA) band, which is used to identify clouds, was used to mask out cloudy pixels from the selected images. All the selected images were combined by the aggregation method, in which mosaic images were produced [37,38]. We collected about 1000 samples from each year's images and randomly divided them into 50% of the training set and 50% of the validation set. The random forest (RF) algorithm was chosen as a classifier. We classified the study area into six types: forest, grassland, cropland, urban and built-up, water, and barren land, and extracted the area occupied by buildings.

3.3.4. Modeling Land Subsidence Based on the GRU

GRU model can learn the relationships of sequence data through a self-cyclic process and can share parameters among several time steps [22]. The self-cyclic structure includes a reset gate r for adjusting the combination of new inputs and the previous hidden state and an update gate z for controlling how much information from the previous hidden state will carry over to the current hidden state. Additionally, update gates are used to adjust the information flow in the unit with the aim that each cycle in the process can adaptively capture correlations at different time scales.

The hidden state $h^{(t)}$ of the GRU at time t involves a linear interpolation between the previous hidden state $h^{(t-1)}$ and the candidate hidden state $\tilde{h}^{(t)}$:

$$h^{(t)} = z\tilde{h}^{(t)} + (1 - z)h^{(t-1)} \quad (1)$$

where an update gate z determines the degree of retention of the previous information based on the current forecasting result. The update gate is computed by

$$z = \sigma(W_z x + U_z h^{(t-1)}) \tag{2}$$

where σ is a sigmoid function with a value between 0 and 1. W_z and U_z are the training weight matrices of z which are learned.

The reset gate r controls how much historical information should be ignored with the expression of

$$r = \sigma(W_r x + U_r h^{(t-1)}) \tag{3}$$

where W_r and U_r are the training weight matrices of the reset gate r . The computation formula of $\tilde{h}^{(t)}$ is similar to that of a traditional recurrent unit:

$$\tilde{h}^{(t)} = \varphi(W x + U(r \cdot h^{(t-1)})) \tag{4}$$

where φ is usually the \tanh activation function with a value from -1 to 1 . The GRU self-cyclic structure is illustrated in Figure 4.

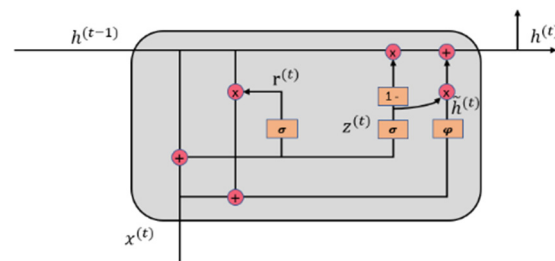


Figure 4. Illustration of gated recurrent units (modified from [22]).

4. Results

4.1. Land Subsidence Distribution and Validation

The leveling benchmarks data were applied to validate the derived land subsidence through InSAR technology. The vertical displacement is considered to be more appropriate for comparison with ground leveling measurements. Thus, the measurements in line of sight are directly projected into the vertical direction. The correlation coefficient between the leveling benchmarks data and the land subsidence derived from SAR images was 0.93 (Figure 5). The absolute errors between the two data were 3 mm/yr from 2003 to 2005 and 7 mm/yr from 2017 to 2019, respectively.

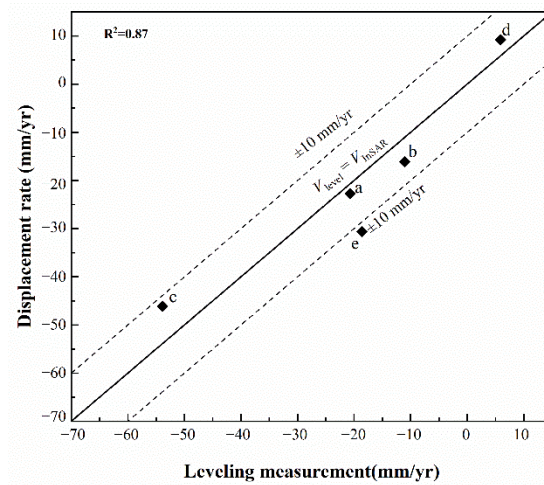


Figure 5. Comparison of subsidence from the leveling benchmarks data and InSAR results.

The maximum vertical displacement rate in the study area was -94 mm/yr from 2003 to 2010, which was located in Tanggu District and marked with a star symbol in Figure 6a. There was a subsidence center in the western Tanggu District. The percentage of PSs in the study area with displacement rates ranging from -40 to -25 mm/yr was $\sim 50\%$. The maximum displacement rate in the study area was -87 mm/yr from 2015 to 2020, which was located in Dagang District and denoted with a star in Figure 6b. The land subsidence center was located in the northeastern Hangu District. Compared with the distribution of land subsidence from 2003 to 2010, the displacement rate decreased in this period.

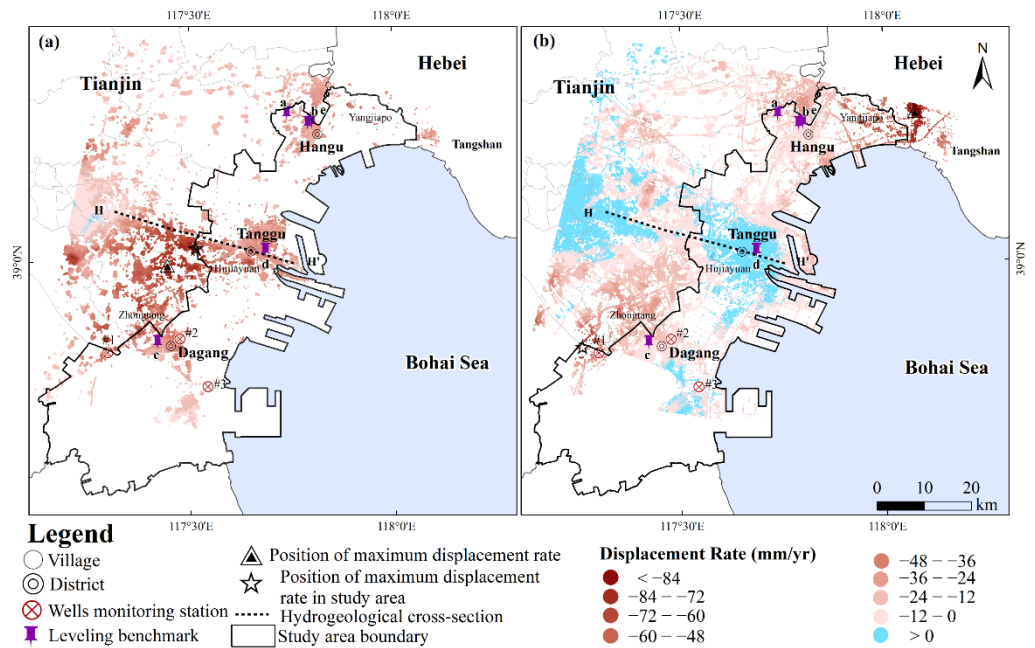


Figure 6. Average vertical displacement rates obtained by the InSAR techniques in the Binhai New Area: (a) SBAS from 2003 to 2010 and (b) PSI from 2015 to 2020. Negative values indicate subsidence, and positive values indicate uplift.

4.2. Area Occupied by Buildings and Validation

With the development of urbanization, the area occupied by buildings has gradually increased. The building distribution derived from the GEE platform is shown in Figure 7. The confusion matrix of the results indicated that the average classification accuracy was 89%.

Buildings are mainly distributed in the middle and southern parts of the study area. The newly built buildings are mainly located in the eastern Tanggu District and southeastern Dagang District, which were coastal industrial zones. The area had a superfiycy of 443.4 km² in 2003, which increased to 756.1 km² in 2020 (Figure 8).

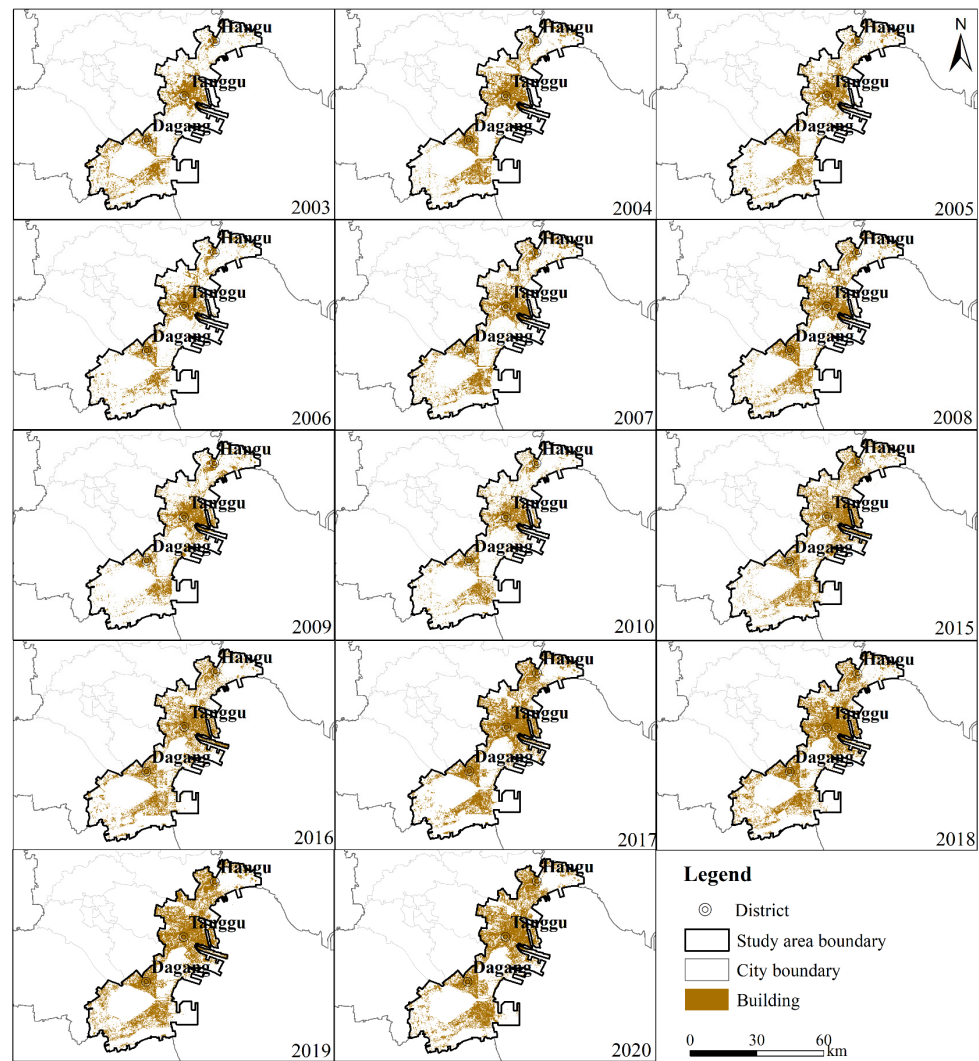


Figure 7. Distribution of buildings in the study area from 2003 to 2010 and 2015 to 2020.

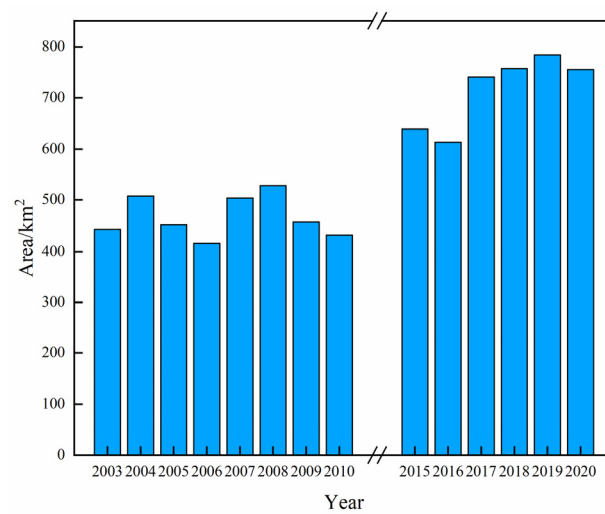


Figure 8. Area occupied by buildings in the Binhai New Area extracted with the GEE from 2003 to 2010 and 2015 to 2020.

5. Discussion

5.1. Relationships between Factors and Land Subsidence

5.1.1. The Groundwater Level and Land Subsidence

According to Terzaghi’s effective stress principle, as the water level drops, the pressure undertaken by the pore water is transferred to the soil, resulting in land subsidence [39]. The contour lines of the groundwater level depth of the second and third confined aquifer groups in 2013, 2016, and 2019 were compared with the subsidence rate distribution from 2015 to 2020 (Figure 9). The distribution of land subsidence was more consistent with the groundwater level depth of the third confined aquifer group. There were two main depression cones of groundwater level, located in the northwestern Hangu District and in Dagang District, which were consistent with the locations of serious land subsidence (Figure 6b). With the decreasing groundwater level depth of the third confined aquifer group in Tanggu District, the land subsidence rate slowed down correspondingly. The subsidence intensified in the region with the increasing groundwater level depth in Hangu District.

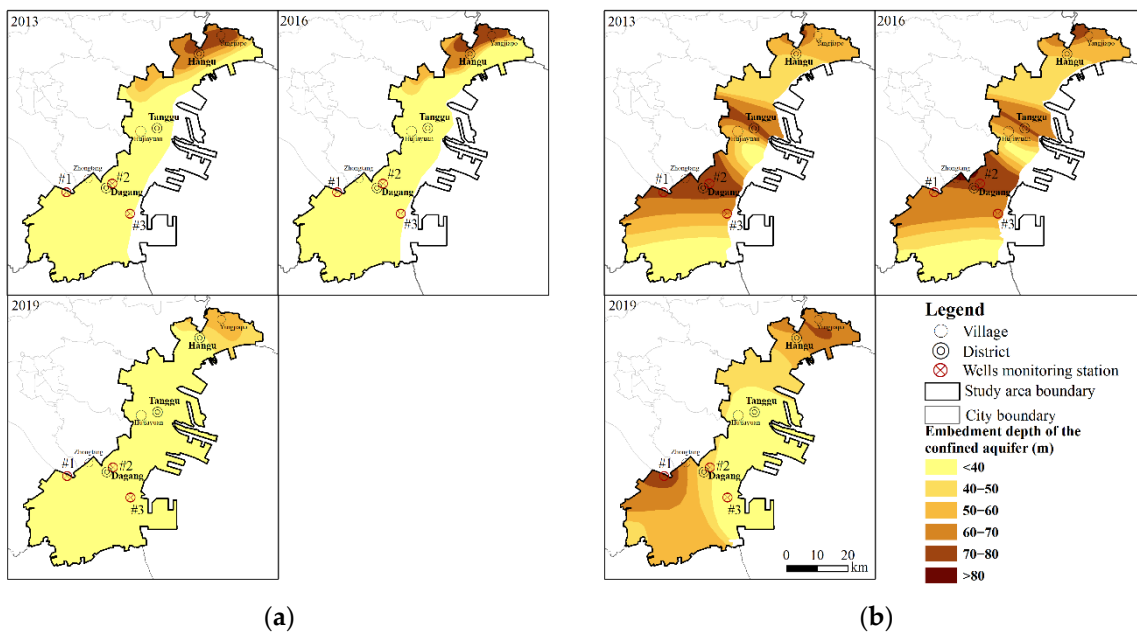


Figure 9. The contour lines of groundwater level depth of the second (a) and third (b) confined aquifer group in 2013, 2016, and 2019.

Three monitoring wells of the third confined aquifer group were chosen to analyze the relationship between groundwater level fluctuation and land subsidence. Well #1 was located in the displacement rate zone from -60 to -48 mm/yr, Well #2 was located in the displacement rate zone from -24 to -12 mm/yr, and Well #3 was located in the -12 to 12 mm/yr displacement rate zone. However, the position of each well does not correspond to any PSs. The average InSAR value of PSs at a distance within 200 m from each well was used as the cumulative subsidence to be compared with the groundwater level. The cumulative average InSAR value of the PSs from January 2018 can be obtained by linear interpolation. Land subsidence exhibited a seasonal pattern, which showed a downward movement from July to January and an upward movement from April to July (Figure 10). The small panel shows the local exaggerated curves of cumulative land subsidence and groundwater level. The exaggeration factors of land subsidence and groundwater level are 2 and 50 times, respectively. The shape of groundwater level fluctuation was similar to that of land subsidence. The absolute value of the Pearson correlation coefficient of groundwater level and cumulative land subsidence of the three wells were 0.45, 0.75, and 0.21, respectively. Considering the hysteresis of the water released from fine sediment

layers, compaction still occurred in the aquifer group, in which land subsidence continued during the groundwater level recovery period, such as the last three months of 2019.

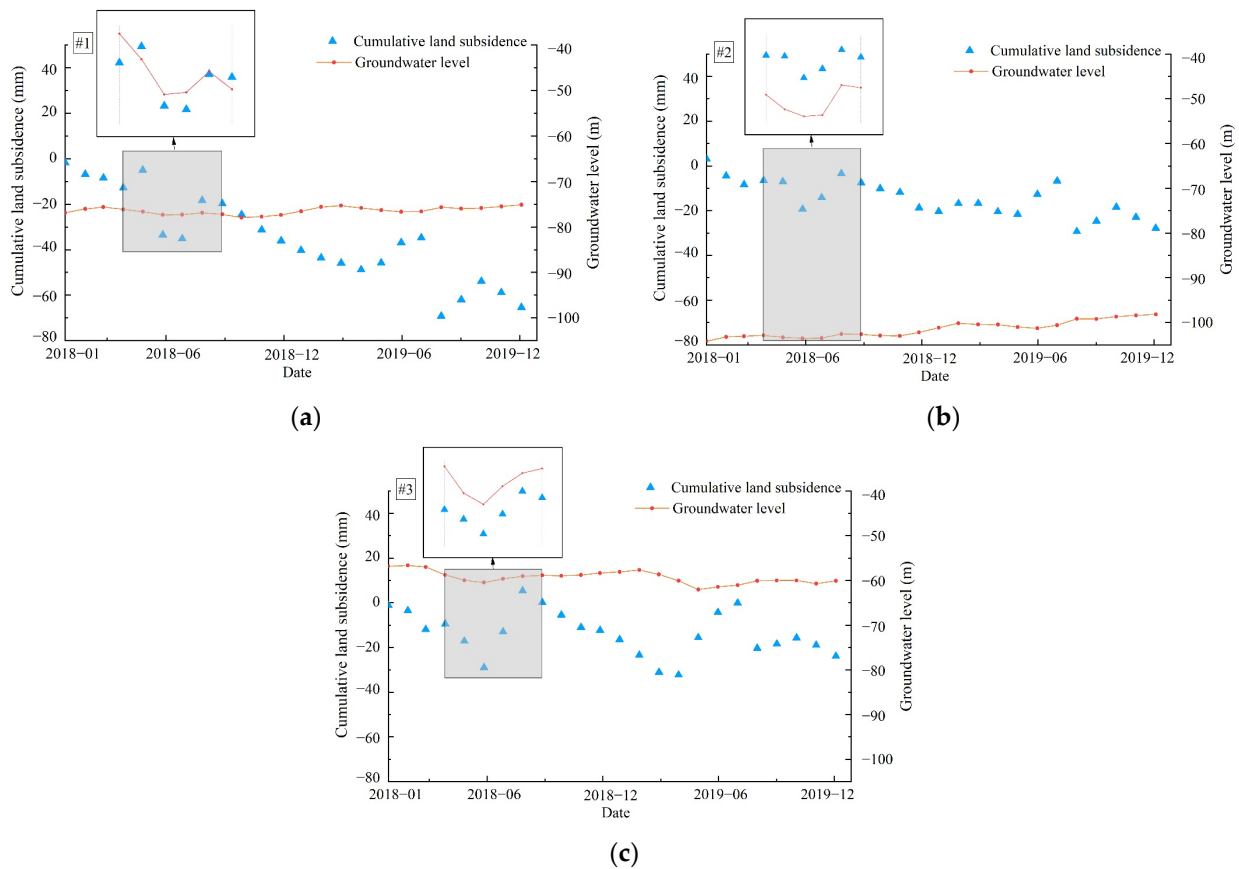


Figure 10. Cumulative land subsidence and groundwater level at typical groundwater monitoring wells: (a) well #1, (b) well #2 and (c) well #3.

5.1.2. Area Occupied by Buildings and Land Subsidence

In the processes of building construction and loading, the increase in additional foundation stress can lead to the compressive deformation of cohesive soil and displacement. The land subsidence cycle is generally 10 years or less [40]. The area occupied by buildings per month and cumulative land subsidence of PSs within a 200 m buffer near three wells were compared (Figure 11). The absolute value of the Pearson correlation coefficient between the cumulative land subsidence and the area occupied by buildings of the three wells were 0.66, 0.52, and 0.26, respectively. New buildings were mainly in the coastal land reclamation areas in the eastern part of Tanggu District and the southeastern part of Dagang District, where the displacement rate ranged from -24 to 0 mm/yr. In the central Tanggu District, there has been a rebound in recent years due to the long-term construction implementation since 2006. In the northeastern part, the area occupied by buildings was almost unchanged, but the land subsidence rate increased due to groundwater extraction for the aquaculture industry [10]. It is noted that the land subsidence of Well #3 has a low correlation with the groundwater level and area occupied by buildings, which may be due to the subsidence caused by land reclamation in the past 10 years since Well #3 is located in the coastal industrial zone.

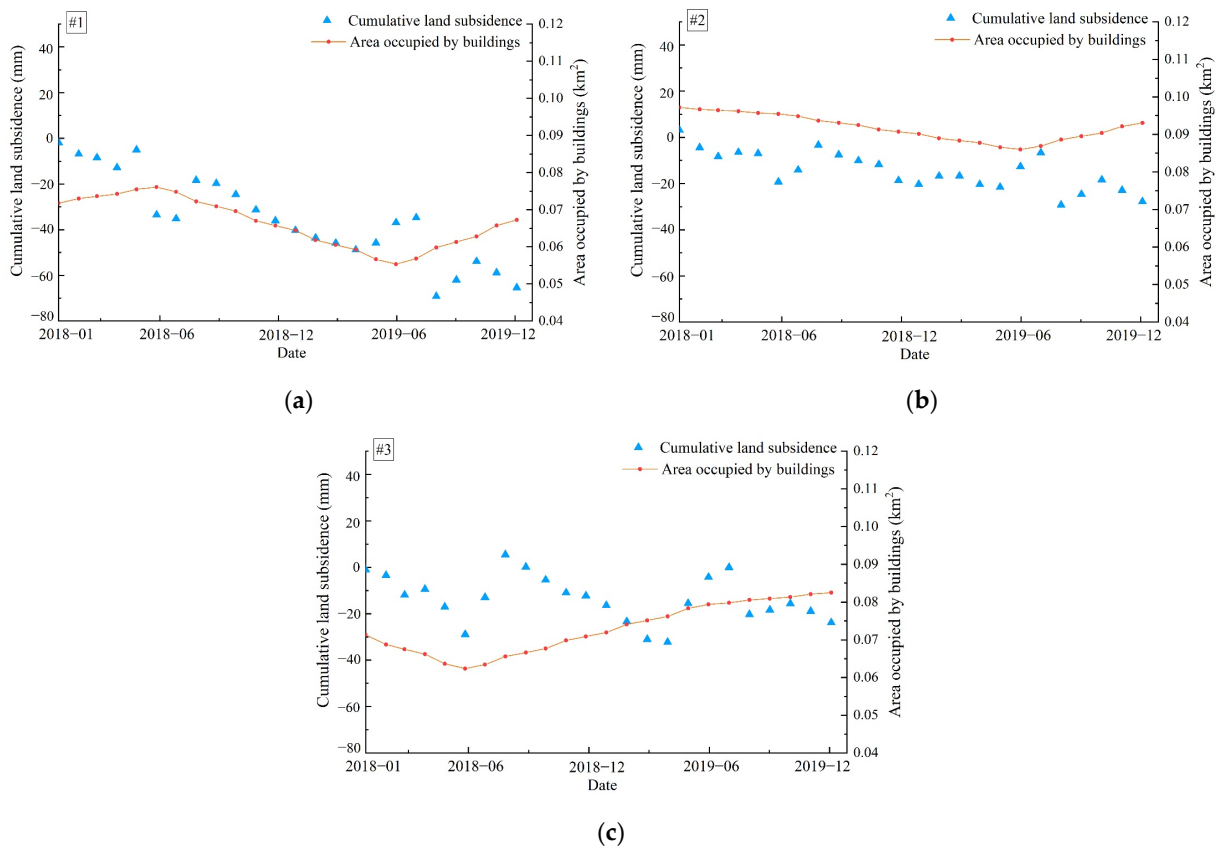


Figure 11. Cumulative land subsidence and area occupied by buildings in the 200 m buffer zone around each well: (a) well #1, (b) well #2 and (c) well #3.

5.1.3. Compressible Layer Thickness and Land Subsidence

The lithology controls the subsidence magnitude and the evolution process [41]. Figure 12 shows the land subsidence from 2003 to 2010 and from 2015 to 2020 along the west-to-east hydrogeological cross-section (H-H') marked in Figure 1. The absolute value of Pearson correlation coefficients between the land subsidence rate and the thickness of the compressible layer was 0.42 from 2003 to 2010 and 0.50 from 2015 to 2020.

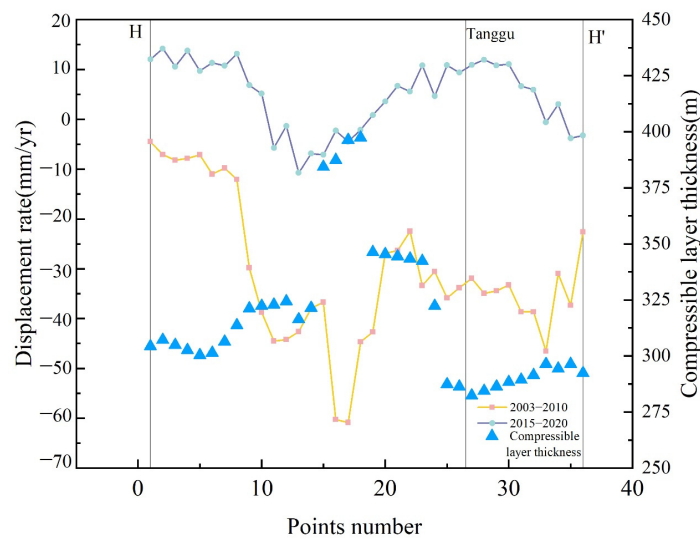


Figure 12. Land subsidence rate and compressed layer thickness along the H-H' profile at the two time periods.

The lithology information at wells #1 and #3 was showed in Figure 13. The thicknesses of the compressible deposits, such as silty clay, clay, and silt, are 234.5 m and 222 m, accounting for 78.1% and 72.5% of the borehole. Since there is no borehole around Well #2, the thickness of compressible deposits was set as the same as that in reference to Yang, J. L. et al. with the value of 212 m through the calculation of soil samples thickness [18]. The cumulative land subsidence of the three wells was -49.2 mm, -33.1 mm, and -15.1 mm from 2003 to 2010 and -114.7 mm, -4.3 mm, and $+21.8$ mm from 2015 to 2020. Due to the large thickness of the compressible deposits, the land subsidence of Well #1 was larger than that of other wells. The land subsidence of Well #2 and Well #3 slowed down, which may be due to the over-consolidation and slight over-consolidation of compressible deposits caused by the long-term construction history and large-scale exploitation of groundwater in the past [18].

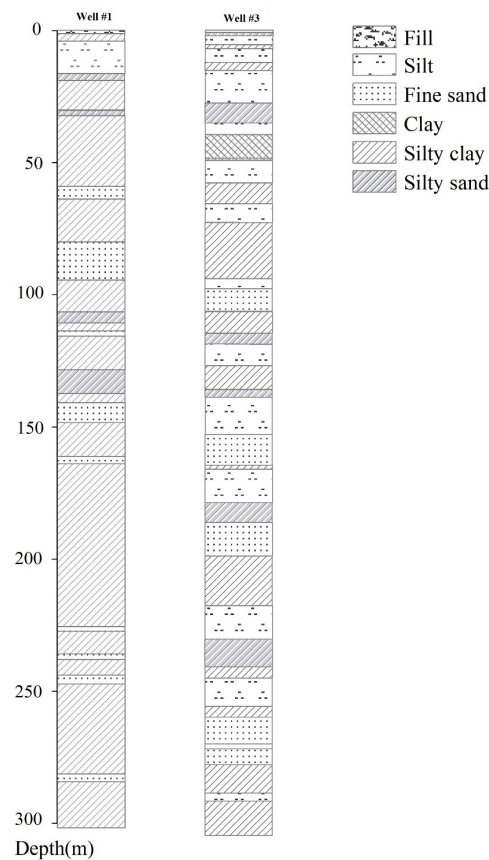


Figure 13. Schematic description of Well #1 and Well #3 lithologies.

5.2. Simulation of Land Subsidence

5.2.1. Construction of the GRU Model

The cumulative average InSAR value of the PSs in the 200 m buffer zone around the well was the output. The analysis in Section 5.1.1 showed that the distribution of land subsidence is more similar to the groundwater level distribution in the third confined aquifer group than in other aquifer groups. Therefore, we calculated the cumulative thickness of the compressible layer above the third confined aquifer group for analysis. Considering the groundwater was exploited most from the third aquifer group, and land subsidence was more similar to the distribution of groundwater level in the third confined aquifer, the static load from buildings represented by the area occupied by buildings per month, the cumulative thickness of the compressible layer above the third confined aquifer and the monthly third confined aquifer groundwater level from January 2018 to December 2019 were selected as the independent input variables of GRU model.

Because the input data and land subsidence have different units, zero-mean normalization was used to standardize the data [42]. The output of the model can be de-standardized to restore the real subsidence value. The data of the first 20 months (from January 2018 to August 2019), which was 80% of the time series of data, was used for the training model. The remaining data from September 2019 to December 2019 were used to validate the subsidence model. Based on the trial-and-error method, the parameters of the GRU model were determined (Table 1).

Table 1. Parameters of the GRU model.

Parameter	Initial Learning Rate	Batch Size	Dropout Rate	Optimizer	RNN Units
Value	0.001	20	0.1	Adam	16

5.2.2. Model Validation

The RMSE and mean absolute error (MAE) between the simulated outputs and SAR-based data from September 2019 to December 2019 were used to validate the GRU model (Table 2). The overall RMSE and MAE of the model were 3.16 mm and 2.19 mm, respectively. The simulated results fit the SAR-based land subsidence well (Figure 14). The maximum error occurred at Well #1 in September 2019, with the reason of land subsidence changing greatly in September and October 2019. The relative larger RMSE and MAE for Well #1 than the values of the other two wells with low land subsidence indicated that the constructed GRU model was sensitive to slow subsidence processes.

Table 2. Comparison between SAR-based values and simulated results for three wells.

Monitoring Well	Displacement (mm)	2019/09	2019/10	2019/11	2019/12	MAE	RSME
#1	InSAR derived	-61.94	-53.83	-58.80	-65.34	4.13	5.00
	Modeled	-52.97	-51.68	-56.43	-62.30		
	Absolute error	8.97	2.15	2.37	3.04		
#2	InSAR derived	-24.66	-18.39	-22.88	-27.83	0.78	0.80
	Modeled	-23.82	-19.3	-22.37	-28.70		
	Absolute error	0.84	0.91	0.51	0.87		
#3	InSAR derived	-18.42	-15.70	-18.95	-23.81	1.65	2.07
	Modeled	-16.12	-15.99	-18.32	-20.44		
	Absolute error	2.3	0.29	0.63	3.37		

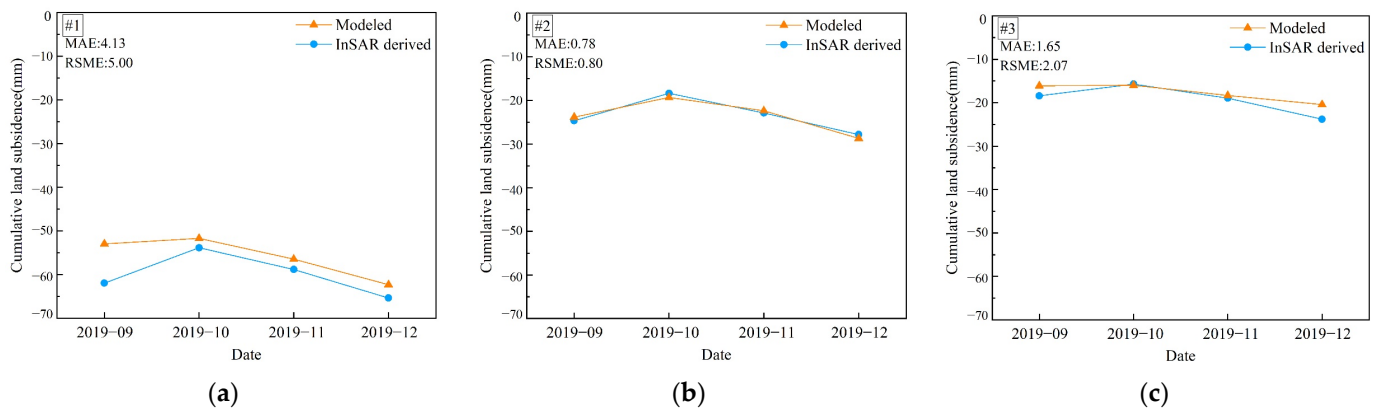


Figure 14. InSAR and simulated values for each monitoring well: (a) well #1, (b) well #2 and (c) well #3.

6. Conclusions

Coastal subsidence is a highly complex problem owing to multiple reasons. The spatial and temporal characterizations of land subsidence in the Tianjin Binhai New Area were obtained by using InSAR technology. The InSAR results were combined with groundwater monitoring data, buildings load, and geological features to analyze the causes of land subsidence, and a GRU model considering the above three factors, which is neglected in traditional data-driven methods, was constructed to simulate land subsidence.

Based on the analysis of land subsidence and three factors, we found that the groundwater level in the third confined aquifer has a stronger correlation to land subsidence than the area occupied by buildings and compressible layer thickness. Seasonal variation in land subsidence is positively correlated with the level of groundwater. The absolute value of the Pearson correlation coefficient of groundwater level and cumulative land subsidence of the three wells were 0.45, 0.75, and 0.21, respectively. The area occupied by buildings per month and land subsidence curves show that an increase in the area occupied by buildings was often accompanied by land subsidence, and the absolute value of the Pearson correlation coefficient between the cumulative land subsidence and the area occupied by buildings of the three wells were 0.66, 0.52 and 0.26, respectively. The results also show that serious land subsidence is generally distributed in regions with thick compressible deposits. The outcomes of this study indicate that a GRU neural network land subsidence model combined with groundwater level, the area occupied by buildings, and the thickness of compressible deposits can be used to predict future land subsidence with a small amount of data in the Binhai New Area and the overall RMSE and MAE of the model were 3.16 mm and 2.19 mm, respectively.

Our study provides a scientific basis for coastal land subsidence prevention and control. In future work, more groundwater level data of aquifers at different depths will be collected, and the features of coastal lithofacies will be fully considered to further explore the simulation of coastal land subsidence.

Author Contributions: Conceptualization, C.L. and L.Z.; Data curation, C.L., D.D. and H.W.; Formal analysis, C.L.; Methodology, X.L., H.G. and P.T.; Resources, D.D.; Software, C.L.; Supervision, L.Z.; Validation, C.L. and L.Z.; Visualization, C.L.; Writing—original draft, C.L.; Writing—review and editing, C.L. and L.Z. All authors have read and agreed to the published version of the manuscript.

Funding: The research work described herein was funded by Natural Science Foundation of Beijing Municipality (Grant No. 8202008).

Institutional Review Board Statement: Not applicable.

Informed Consent Statement: Not applicable.

Data Availability Statement: The Sentinel-1A/B and Envisat ASAR data are freely available from the European Space Agency. The Landsat data are freely available from the United States Geological Survey. The 30-meter resolution DEM data can download from the Shuttle Radar Topography Mission. The datasets generated during and/or analyzed in this study are available from the corresponding author upon reasonable request.

Acknowledgments: The authors thank Hanrui Sun of the College of Resource Environment and Tourism, Capital Normal University, for the provided GRU algorithm assistance.

Conflicts of Interest: The authors declare no conflict of interest. The funders had no role in the design of the study; in the collection, analyses, or interpretation of data; in the writing of the manuscript; or in the decision to publish the results.

References

1. Herrera-García, G.; Ezquerro, P.; Tomás, R.; Béjar-Pizarro, M.; López-Vinielles, J.; Rossi, M.; Mateos Rosa, M.; Carreón-Freyre, D.; Lambert, J.; Teatini, P.; et al. Mapping the global threat of land subsidence. *Science* **2021**, *371*, 34–36. [[CrossRef](#)] [[PubMed](#)]
2. Hu, B.; Zhou, J.; Xu, S.; Chen, Z.; Wang, J.; Wang, D.; Wang, L.; Guo, J.; Meng, W. Assessment of hazards and economic losses induced by land subsidence in Tianjin Binhai new area from 2011 to 2020 based on scenario analysis. *Nat. Hazards* **2013**, *66*, 873–886. [[CrossRef](#)]

3. Felsenstein, D.; Lichter, M. Social and economic vulnerability of coastal communities to sea-level rise and extreme flooding. *Nat. Hazards* **2014**, *71*, 463–491. [[CrossRef](#)]
4. Haley, M.; Ahmed, M.; Gebremichael, E.; Murgulet, D.; Starek, M. Land subsidence in the Texas coastal bend: Locations, rates, triggers, and consequences. *Remote Sens.* **2022**, *14*, 192. [[CrossRef](#)]
5. Ferretti, A.; Prati, C.; Rocca, F. Nonlinear Subsidence Rate Estimation Using Permanent Scatterers in Differential SAR Interferometry. *IEEE Trans. Geosci. Remote Sens.* **2000**, *38*, 2202–2212. [[CrossRef](#)]
6. Berardino, P.; Fornaro, G.; Lanari, R.; Sansosti, E. A New Algorithm for Surface Deformation Monitoring Based on Small Baseline Differential SAR Interferograms. *IEEE Trans. Geosci. Remote Sens.* **2002**, *40*, 2375–2383. [[CrossRef](#)]
7. Teatini, P.; Strozzi, T.; Tosi, L.; Wegmüller, U.; Werner, C.; Carbognin, L. Assessing short-and long-time displacements in the Venice coastland by synthetic aperture radar interferometric point target analysis. *J. Geophys. Res. Earth Surf.* **2007**, *112*, F01012. [[CrossRef](#)]
8. Ng, A.H.-M.; Ge, L.; Li, X.; Abidin, H.Z.; Andreas, H.; Zhang, K. Mapping land subsidence in Jakarta, Indonesia using persistent scatterer interferometry (PSI) technique with ALOS PALSAR. *Int. J. Appl. Earth Obs. Geoinf.* **2012**, *18*, 232–242. [[CrossRef](#)]
9. Lu, W.; Han, C.; Yue, X.; Zhao, Y.; Zhou, G. Land Subsidence Monitoring in Tianjin with PS-InSAR Technique based on Sentinel-1 Data. *Remote Sens. Technol. Appl.* **2020**, *35*, 8.
10. Huang, X.M.; Guo, Q.Q.; Wen, F.T. Land Subsidence Monitoring in Tianjin Binhai New Area Based on Sentinel-1 Data. *J. Beijing Polytech. Coll.* **2019**, *18*, 5. [[CrossRef](#)]
11. Törnqvist, T.E.; Wallace, D.J.; Storms, J.E.; Wallinga, J.; Van Dam, R.L.; Blaaauw, M.; Derksen, M.S.; Klerks, C.J.; Meijneken, C.; Sniijders, E. Mississippi Delta subsidence primarily caused by compaction of Holocene strata. *Nat. Geosci.* **2008**, *1*, 173–176. [[CrossRef](#)]
12. Teatini, P.; Tosi, L.; Strozzi, T. Quantitative evidence that compaction of Holocene sediments drives the present land subsidence of the Po Delta, Italy. *J. Geophys. Res. Solid Earth* **2011**, *116*, B08407. [[CrossRef](#)]
13. Qu, F.F.; Lu, Z.; Zhang, Q.; Bawden, G.W.; Kim, J.W.; Zhao, C.Y.; Qu, W. Mapping ground deformation over Houston–Galveston, Texas using multi-temporal InSAR. *Remote Sens. Environ.* **2015**, *169*, 290–306. [[CrossRef](#)]
14. Van Asselen, S.; Erkens, G.; Stouthamer, E.; Woolderink, H.A.; Geeraert, R.E.; Hefting, M.M. The relative contribution of peat compaction and oxidation to subsidence in built-up areas in the Rhine-Meuse delta, The Netherlands. *Sci. Total Environ.* **2018**, *636*, 177–191. [[CrossRef](#)] [[PubMed](#)]
15. Wu, T.J.; Cui, X.D. Study and comprehensive treatment of land subsidence in Tianjin. *Hydrogeol. Eng. Geol.* **1998**, *25*, 4.
16. Zhang, T.X.; Shen, W.B.; Wu, W.H.; Zhang, B.; Pan, Y.J. Recent surface deformation in the Tianjin area revealed by Sentinel-1A data. *Remote Sens.* **2019**, *11*, 130. [[CrossRef](#)]
17. Guo, J.M.; Hu, J.Y.; Li, B.; Zhou, L.; Wang, W. Land subsidence in Tianjin for 2015 to 2016 revealed by the analysis of Sentinel-1A with SBAS-InSAR. *J. Appl. Remote Sens.* **2017**, *11*, 026024. [[CrossRef](#)]
18. Yang, J.; Cao, G.; Han, D.; Yuan, H.; Hu, Y.; Shi, P.; Chen, Y. Deformation of the aquifer system under groundwater level fluctuations and its implication for land subsidence control in the Tianjin coastal region. *Environ. Monit. Assess.* **2019**, *191*, 1–14. [[CrossRef](#)]
19. Zhu, L.; Gong, H.L.; Li, X.J.; Li, Y.Y.; Su, X.S.; Guo, G.X. Comprehensive analysis and artificial intelligent simulation of land subsidence of Beijing, China. *Chin. Geogr. Sci.* **2013**, *23*, 237–248. [[CrossRef](#)]
20. Shi, L.Y.; Gong, H.L.; Chen, B.B.; Zhou, C.F. Land Subsidence Prediction Induced by Multiple Factors Using Machine Learning Method. *Remote Sens.* **2020**, *12*, 4044. [[CrossRef](#)]
21. Hochreiter, S.; Schmidhuber, J. Long short-term memory. *Neural Comput.* **1997**, *9*, 1735–1780. [[CrossRef](#)] [[PubMed](#)]
22. Cho, K.; Van Merriënboer, B.; Gulcehre, C.; Bahdanau, D.; Bougares, F.; Schwenk, H.; Bengio, Y. Learning phrase representations using RNN encoder-decoder for statistical machine translation. *arXiv* **2014**, arXiv:1406.1078. [[CrossRef](#)]
23. Li, H.J.; Zhu, L.; Dai, Z.X.; Gong, H.L.; Guo, T.; Guo, G.X.; Wang, J.B.; Teatini, P. Spatiotemporal modeling of land subsidence using a geographically weighted deep learning method based on PS-InSAR. *Sci. Total Environ.* **2021**, *799*, 149244. [[CrossRef](#)]
24. LeCun, Y.; Bengio, Y.; Hinton, G. Deep learning. *Nature* **2015**, *521*, 436–444. [[CrossRef](#)] [[PubMed](#)]
25. Li, L.B.; GONG, X.N.; Gan, X.L.; Cheng, K.; Hou, Y.M. Prediction of maximum ground settlement induced by shield tunneling based on recurrent neural network. *China Civ. Eng. J.* **2020**, *S01*, 7.
26. Hu, R.L.; Yue, Z.Q.; Wang, L.C.; Wang, S.J. Review on current status and challenging issues of land subsidence in China. *Eng. Geol.* **2004**, *76*, 65–77. [[CrossRef](#)]
27. Xiao, G.Q. Study on Mechanism of Clayey Soil by High Pressure Consolidation and Process of Land Subsidence: A Case Study of the G2 Geologic Drill-Hole in Tianjin Binhai New Area. Ph.D. Thesis, China University of Geosciences, Wuhan, China, 2014.
28. Ha, D.; Zheng, G.; Loáiciga, H.A.; Guo, W.; Zhou, H.Z.; Chai, J.C. Long-term groundwater level changes and land subsidence in Tianjin, China. *Acta Geotech.* **2021**, *16*, 1303–1314. [[CrossRef](#)]
29. Zhang, Z.J. *Atlas of Groundwater Sustainable Utilization in North China Plain*, 1st ed.; China Cartographic Publishing House: Beijing, China, 2009.
30. Dong, K.G.; Wang, W.; Yu, Q.; Lu, Y. History and enlightenment of land subsidence controlling in Tianjin City. *Chin. J. Geol. Hazard Control* **2008**, *19*, 6. [[CrossRef](#)]
31. Yi, L.X.; Zhang, F.; Xu, H.; Chen, S.J.; Wang, W.; Yu, Q. Land subsidence in Tianjin, China. *Environ. Earth Sci.* **2011**, *62*, 1151–1161. [[CrossRef](#)]

32. Liu, H.P. The study on the land subsidence with the affect of high-rise buildings in Tianjin Binhai New Area. Ph.D. Thesis, Chang'an University, Xi'an, China, 2010.
33. Ferretti, A.; Prati, C.; Rocca, F. Permanent scatterers in SAR interferometry. *IEEE Trans. Geosci. Remote Sens.* **2001**, *39*, 8–20. [[CrossRef](#)]
34. Werner, C.; Wegmuller, U.; Strozzi, T.; Wiesmann, A. Interferometric point target analysis for deformation mapping. In Proceedings of the IGARSS 2003. 2003 IEEE International Geoscience and Remote Sensing Symposium. Proceedings (IEEE Cat. No. 03CH37477), Toulouse, France, 21–25 July 2003; pp. 4362–4364.
35. Strozzi, T.; Wegmuller, U.; Tosi, L.; Bitelli, G.; Spreckels, V. Land subsidence monitoring with differential SAR interferometry. *Photogramm. Eng. Remote Sens.* **2001**, *67*, 1261–1270.
36. Phan, T.N.; Kuch, V.; Lehnert, L.W. Land Cover Classification using Google Earth Engine and Random Forest Classifier—The Role of Image Composition. *Remote Sens.* **2020**, *12*, 2411. [[CrossRef](#)]
37. Beckschäfer, P. Obtaining rubber plantation age information from very dense Landsat TM & ETM+ time series data and pixel-based image compositing. *Remote Sens. Environ.* **2017**, *196*, 89–100. [[CrossRef](#)]
38. Richards, D.R.; Belcher, R.N. Global changes in urban vegetation cover. *Remote Sens.* **2019**, *12*, 23. [[CrossRef](#)]
39. Terzaghi, K. Principles of soil mechanics, IV—Settlement and consolidation of clay. *Eng. News-Rec.* **1925**, *95*, 874–878.
40. Zhang, Y.Q.; Yang, X.A.; Zhang, H.T. Analysis of factors influencing land subsidence in tianjin coastal zone. *Ground Water* **2013**, *35*, 2.
41. Khakim, M.Y.; Tsuji, T.; Matsuoka, T. Lithology-controlled subsidence and seasonal aquifer response in the Bandung basin, Indonesia, observed by synthetic aperture radar interferometry. *Int. J. Appl. Earth Obs. Geoinf.* **2014**, *32*, 199–207. [[CrossRef](#)]
42. Zill, D.G. *Advanced Engineering Mathematics*; Jones & Bartlett Publishers: Boston, MA, USA, 2020.